Note: This is a preprint of a paper being submitted for publication. Contents of this paper should not be quoted nor referred to without permission of the author(s).

SPECIES-RESOLVED IMAGING AND GATED PHOTON COUNTING SPECTROSCOPY OF LASER ABLATION PLUME DYNAMICS DURING KrF- AND ArF-LASER PLD OF AMORPHOUS DIAMOND FILMS

David B. Geohegan and A. A. Puretzky*

Solid State Division
Oak Ridge National Laboratory

*Institute of Spectroscopy
Russian Academy of Sciences, Troitsk, Russia

December 1995

SPECIES-RESOLVED IMAGING AND GATED PHOTON COUNTING SPECTROSCOPY OF LASER ABLATION PLUME DYNAMICS DURING KrF- AND ArF-LASER PLD OF AMORPHOUS DIAMOND FILMS

DAVID B. GEOHEGAN AND ALEXANDER A. PURETZKY*
Solid State Division, Oak Ridge National Laboratory, Oak Ridge, TN 37831-6056, odg@ornl.gov
*Institute of Spectroscopy, Troitsk, Russia

ABSTRACT

Gated photon counting spectroscopy and species-resolved ICCD photography have been applied to study the weak plasma luminescence which occurs following the propagation of the initial ablation plume in vacuum and during the 'rebound' of the plume with a substrate during pulsed laser deposition of amorphous diamond. These time- and spatially-resolved spectroscopic techniques were required in order to investigate notable differences between amorphous diamond-like carbon films formed by pulsed laser deposition from ArF (193 nm) and KrF (248 nm) irradiation of pyrolytic graphite in vacuum. Three principal regions of plume emission have been characterized: (1) a bright luminescent ball (v ~3–5 cm/μs) displaying nearly entirely C^+ emission which appears to result from laser interaction with the initial ejecta, (2) a spherical ball of emission (v ~1 cm/μs) displaying neutral carbon atomic emission lines and, at early times, jets of excited C_2, and (3) a well-defined region of broadband emission (v ~ 0.3 cm/μs) near the target surface first containing emission bands from C_2, then weak, continuum emission thought to result from C_3 and higher clusters and/or blackbody emission from hot clusters or nanoparticles. For both lasers, the measurements reveal an explosive interaction within the plume which results in a variety of new gas dynamic observations *in vacuum*:. These include (a) generation of instabilities or jets, (b) confinement of a residual part of the plume near the pellet surface, (c) cluster formation in the collisional, confined regions of the plume, and (d) reflection of the confined region backward to splash and redeposit on the pellet surface. Evidence for gas-phase formation of these clusters in vacuum is indicated from the dynamic evolution of the same cluster bands observed during the collision of the plume with the substrate surface during film growth. Addition of background gases strongly enhances the third (cluster) component, in accordance with plume-splitting phenomena. The combination of sensitive imaging and photon-counting diagnostic techniques permit an understanding of the importance of gas dynamic effects, such as clustering, on the time-of-flight distributions of species arriving during the deposition of thin films in both vacuum and background gases.

INTRODUCTION

Recently, a new amorphous form of diamond has been grown in thin film form by filtered vacuum arc[1] and pulsed laser deposition[2–12] techniques. This new allotrope of pure carbon is distinguished from the diamond-like hydrogenated carbons (a-C:H) by the term tetrahedrally coordinated amorphous carbon (*ta*-C)[1] or amorphic diamond.[2–5] In its purest form, the disordered tetrahedral carbon is almost entirely sp^3 bonded and has a density, hardness, and electrical resistivity near that of natural diamond.

Films with the highest sp^3:sp^2 ratios exhibit very high compressive stresses, which limits maximum thicknesses to ~1 μm. Indeed the diamond-like bonding is thought to arise from the compressive stress generated by the shallow implantation of carbon ions during film deposition, which is believed to drive the effective temperature and pressure conditions to a point well inside the stable diamond phase.[1]

Pulsed laser deposition (PLD) of *ta*-C is accomplished by laser ablation of graphite in vacuum onto unheated substrates. While it is true that at a given laser wavelength the highest quality films are usually obtained at the highest achievable irradiance, the laser wavelength plays an even greater role. Ablation of graphite using infrared lasers (Nd:YAG, 1064 nm) requires intensities > 10^{10} W/cm^2 to produce ~70% sp^3-bonded *ta*-C, while higher quality films are obtained using ultraviolet

(notably 248 nm and 193 nm) laser irradiation at much lower intensities. The highest quality (84–95%sp^3-bonded) ta-C films grown by PLD require ArF-laser (193 nm) intensities of less than 5×10^8 W/cm^2.[9-12]

Recently, a comparative study of ArF- (193 nm) and KrF-(248 nm) laser deposited diamond-like films was performed and correlated with gated-ICCD imaging, optical spectroscopic and ion current probe diagnostics of the corresponding laser-generated carbon plasmas.[11,12] Higher quality DLC films were obtained using ArF-laser irradiation compared to KrF-laser PLD, as determined by EELS and spectroscopic ellipsometry analysis.

The in situ diagnostics revealed several key similarities and differences between the plasmas generated by these two lasers. Briefly, three distinct components to the 'plume' transport were revealed by these first sensitive (full-spectrum) photographic images. The diamond-like film properties were shown to depend on maximizing the fast (bright) ion component and minimizing the slower two (weakly emitting) components.

In this paper, gated photon counting spectroscopy is coupled with spectroscopic imaging in order to characterize the very weak optical emission emanating from the second and third components during expansion into vacuum. Previously, gated photon counting and ICCD imaging were jointly employed to investigate the expansion and time-resolved blackbody emission spectra of hot particulates ejected from YBCO and BN targets following excimer laser ablation into vacuum.[13,14] Similarly, in this case, the spatially- and temporally-localized 'components' of emission revealed by the ICCD images are separately studied.

Furthermore, imaging will be presented to outline a strong (explosive) gas dynamic interaction between the rapidly expanding ion ball and the residual plume which appears responsible for the formation of (i) the confined region of luminescence near the target which moves backward to reflect and splash across the pellet surface in a characteristic "footprint" pattern, and (ii) the turbulent "jets" or instability in the forward direction due to strong interplume interaction. The confinement and reflection of the third component at the target surface dramatically increases the number of collisions within this region of the plume, resulting in effective cluster formation. A detailed description of these new interplume dynamics will be published elsewhere.

In addition, the weak 'rebound' luminescence near the substrate surface has been spectrally resolved and imaged. The results indicate that gas-phase clustering of C-atoms into C_2, C_3 and higher clusters occurs in the 'stagnation layer' above the substrate surface, where incoming and reflected fluxes collide. The emission spectra show a remarkable similarity to that of the clusters in the detrimental, slow third component. Incorporation of both fluxes of clusters in the film may be a limitation for high-quality amorphous diamond material.

Finally, addition of background argon is shown to greatly enhance cluster growth in the third component of the carbon plume. *Three* components are similarly observed in the ion probe signal, the first two in accordance with the 'plume splitting' effect detailed elsewhere[15-17] and the third appears correlated with the cluster emission studied here and noted elsewhere[18,19] for other materials. Clustering via laser ablation of graphite into high pressure background gases has been imaged previously[18,19], and exploited for the production of fullerenes. This third component to the ablated flux in low-pressure background argon appears to be a similar gas-dynamic effect.

EXPERIMENTAL

The experimental set up has been described previously.[11-19] It consists of a stainless steel high vacuum chamber (40 cm diameter) equipped with Suprasil quartz windows for optical diagnostics. The chamber is pumped by a turbomolecular pump to a base pressure of 5×10^{-7} Torr. A Questek (Model 2960) excimer laser operating on ArF (19 ns FWHM, 600 mJ) or KrF (29 ns FWHM, 900 mJ) was used. The beam was apertured and focused into the chamber with a spherical lens (500 mm f.l. at 248 nm, 445 mm f.l. at 193nm) to a rectangular beam spot (0.18 cm $\times$ 0.11 cm) at an incidence angle of 30° onto 1"-diameter pyrolytic graphite pellets (Specialty Minerals Inc., less than 10 ppm total impurities). The pellets were rotated during the film deposition and plasma plume diagnostics experiments. The maximum laser fluences at the pellet surface were 7 J/cm^2 (ArF) and 20 J/cm^2 (KrF).
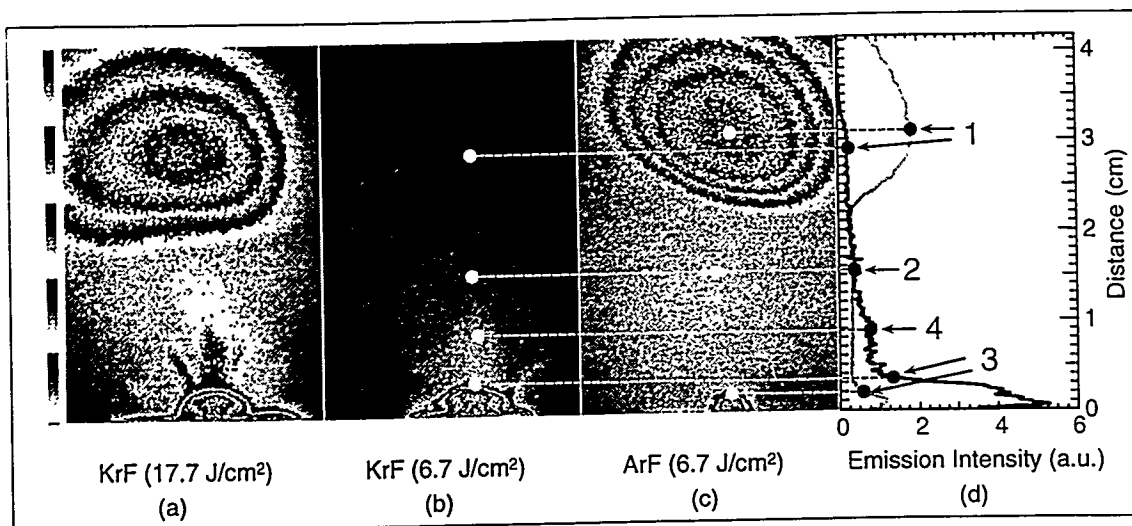
Fig.1. Gated-ICCD photographs of the total visible luminescence at Δt = 800–850 ns following ablation of pyrolytic graphite in vacuum using (a) KrF-laser (17.7 J/cm^2), (b) KrF-laser (6.7 J/cm^2) and (c) ArF-laser (6.7 J/cm^2) irradiation (incident angle 30° from the left). The 5-grayscale palette (shown at the left) is normalized to the maximum numbers of counts for each image. (d) A line-profile of the emission intensity from the irradiated spot along the target normal shows the relative emission intensities of the different plasma components for (1) the fast, ball-shaped component of Fig.1(c) and the shell-shaped component in Fig.1(b); (2) the slower 'second' component of atomic emission; (3) the even slower 'third' component near the target surface and (4) the jets of C_2 which extend between the third and second components. The line profiles are normalized to the intensity of the 2nd-component.

Gated imaging was performed with an intensified charge-coupled device (ICCD), lens-coupled camera system (Princeton Instruments) with variable gain and gate width (5-ns minimum) and a spectral range from 200-820 nm. A tunable (400–720 nm) narrow-band (5 nm FWHM) liquid crystal filter (VariSpec, Cambridge Research & Instrumentation, Inc.) was coupled to the Nikon 105mm lens for species-resolved imaging.

Spectroscopic measurements of the plume luminescence were made with a 1.33-meter spectrometer (McPherson 209) equipped with an 1800 g/mm holographic grating (dispersion 0.5 nm/mm at the exit slit). For gated photon counting, a fast photomultiplier (Hamamatsu R943-02 with gated socket) was coupled to the monochromator exit slit. The output was preamplified by a factor of 100 (EG&G Ortec VT120A), then discriminated and counted by a photon counting unit (Stanford Research Systems, SR400). For measurements close to the pellet, the photomultiplier was gated off during the initial period (~200 ns) of extremely bright plasma emission. Photons were then collected during two gates of arbitrary width and delay following the laser pulse. For each laser pulse, representative dark counts were also independently collected and stored using two identical gates delayed by ~20 ms. Typically, detected photons from 25 laser shots were averaged and stored at each wavelength along with the standard deviations. The resulting spectrum was then corrected for the wavelength response of the optical elements using a correction curve obtained with a calibrated tungsten-halogen lamp.

RESULTS AND DISCUSSION

Gated imaging of the laser ablation of graphite exposes a set of striking transport phenomena which are not readily apparent using mass spectrometric or optical spectroscopic time-of-flight techniques. This is due to the extreme (photon-counting) sensitivity of the intensified CCD-array camera system, and its ability to collect photons from all wavelengths (e.g., from weak continua) simultaneously. In addition, slow-moving or scattered components of the laser-sputtered flux, such as redeposited material, are not overlooked.
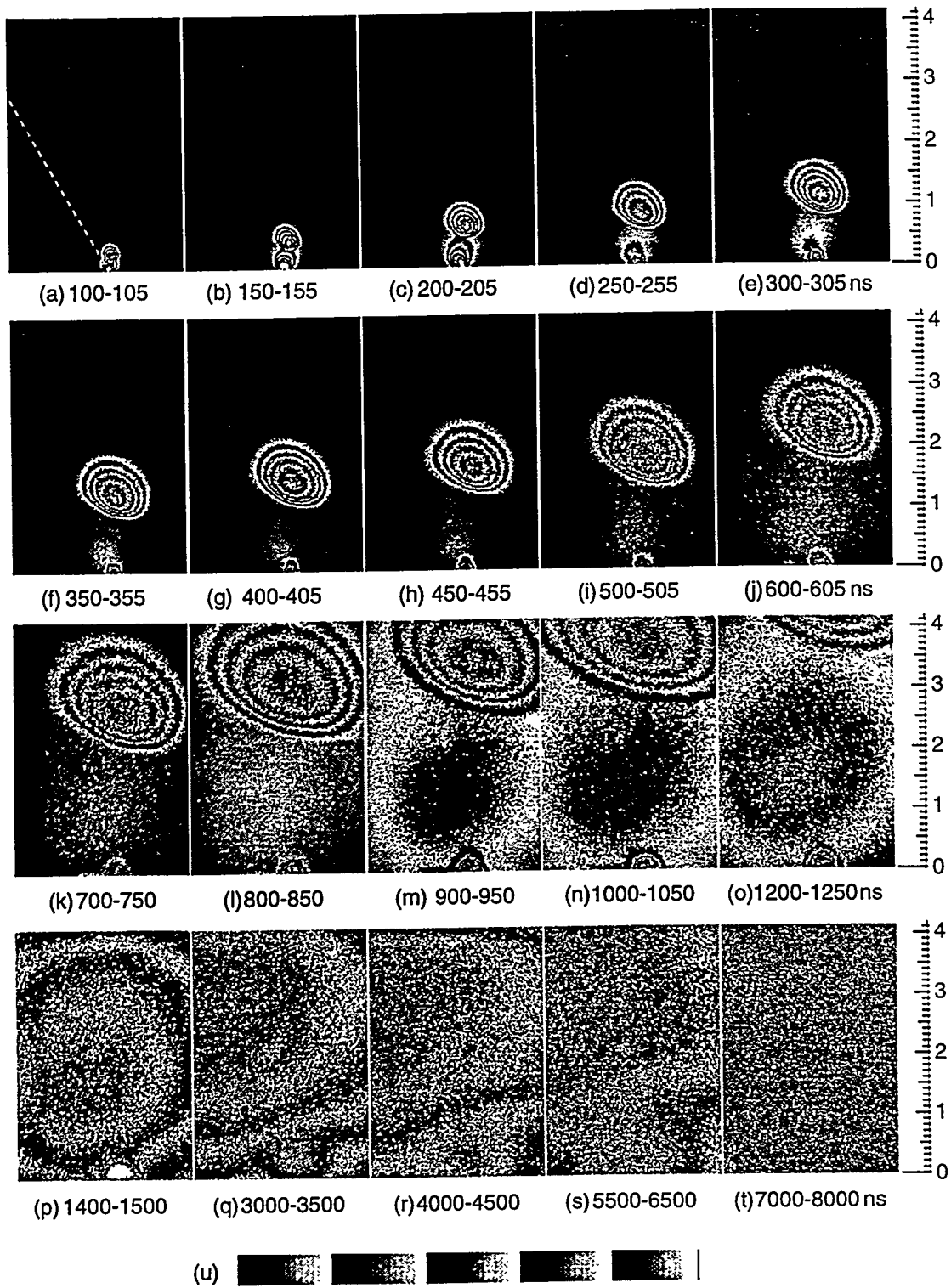
Fig.2. Gated-ICCD images of ArF-laser generated (6.7 J/cm^2) plasmas taken at the indicated times [i.e. from (a) 100 ns delay, 5 ns-gate to (t) 7000 ns delay, 1000 ns-gate] following the laser pulse. (u) The 5-grayscale palette is normalized to the maximum emission intensity of the 1st-plasma component for images (a)-(o), and to the maximum of the 2nd component for (p)-(t). Figure 2(l) and Fig. 1(c) are the same. Laser incidence angle was 30° [from the left, see dashed line in (a)].
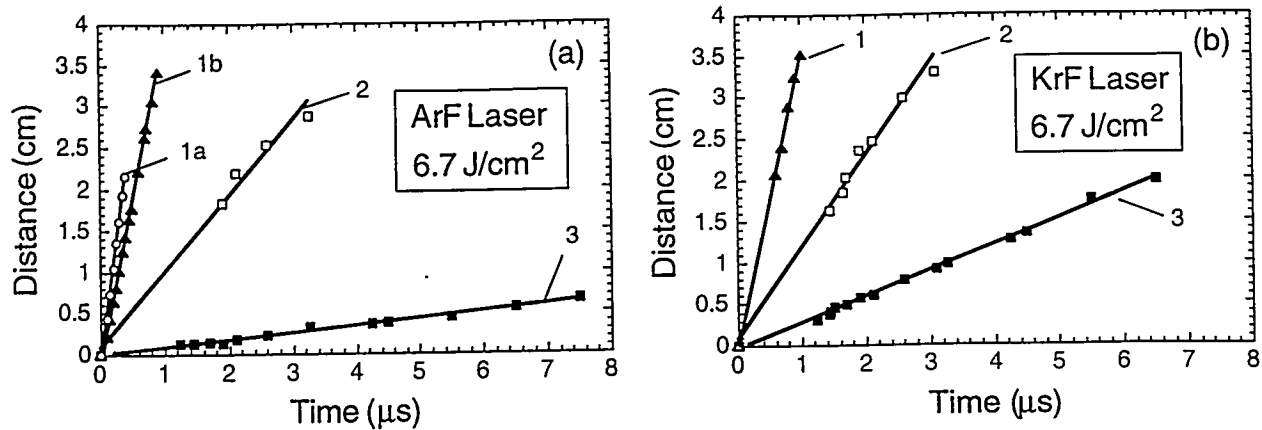
Fig.3. (a) R-t (distance versus time) plots of the propagation of the 1st, 2nd and 3rd plasma components along the normal to the pyrolytic graphite target in vacuum following ArF-laser (6.7 J/cm²) ablation [see Figs.1(c), 1(d), and Fig. 2]. The lines labeled 1b (slope 3.9 cm/μs), 2 (slope 0.9 cm/μs) and 3 (slope 0.08 cm/μs) correspond to linear fits of the propagation emission intensity maxima positions for the 1st, 2nd and 3rd plasma components, respectively. The line 1a (slope 5.5 cm/μs) traces the position of the leading edge (defined as 10% of the maximum emission intensity) of the first component. (b) Propagation of the 1st (slope 3.5 cm/μs) , 2nd (slope 1.1 cm/μs) and 3rd (slope 0.3 cm/μs) plasma components for the KrF-laser (6.7 J/cm²) generated plasma [see Fig.1 (b)].

The principal components observed in the plume luminescence from KrF- and ArF-laser ablated pyrolytic graphite in vacuum are summarized in Figure 1. Three common components exist in different proportions for each image: (1) a fast ball or shell of luminescence centered at d ~3 cm from the target (v_{center} ~3.7 cm/μs, correlated with atomic ions, KE_{C+} ~85 eV); (2) a second, broad ball of luminescence which travels at v_{center} ~ 1.0 cm/μs, (correlated with carbon neutrals, KE_C ~6 eV); and (3) a third region of slowly-propagating luminescence attached to the pellet surface and extending out to d = 2.5 mm (v ~ 0.1–0.3 cm/μs, which will be shown to contain carbon dimers, trimers and higher clusters, e.g. KE_{C_3} ~ 0.2–1.7 eV).

The KrF- and ArF-laser generated plumes at an equal ablation energy density of 6.7 J/cm² are compared in Figs. 1(b)–1(d). As shown in the line profile in Fig. 1(d), the ArF-generated plume emission is dominated by the ionic emission in the fast first component, while the KrF-generated plume exhibits only a weakly-emitting shell at this distance. By contrast, the KrF-plume is dominated by the slow emission in the third component while this component is minimized in the ArF-plume. For each case, an increase in laser energy resulted in increased luminescence of the first component relative to that of the third component, as well as more diamond-like films.[11,12]

In addition, the KrF-plumes exhibit emission from jets of excited C_2 $(d^3\Pi_g)$ (labeled 4 in Fig. 1) which extend from the target surface into the center of the second component at early times. These jets are remarkably reproducible from shot-to-shot and may be correlated with an instability inherent in the simultaneous expansion of the multicomponent plasma. The jets, or instability, are more apparent at higher KrF-laser energy densities as shown in Fig. 1(a), and are not as readily observed in ArF-generated plumes.

Correlation of the plume components with the diamond-like film properties shows that although comparable ionization to that of ArF-laser plasmas can be achieved in the first component by using higher KrF-laser energies, the presence of a pronounced third component (containing C_2, C_3 and higher clusters, as shown below) remains a limiting factor for KrF-deposited films.

A complete sequence of images for the ArF-laser generated plasma plume propagation is given in Fig. 2. The luminous ball of ionic emission (first component) is formed within the region of bright continuum emission near the target surface during the ArF-laser pulse (which begins at 0 ns, peaks at 28 ns, and is essentially done at 60 ns). Between 60 and 100 ns after the pulse initiation, the ball becomes distinguishable from the bright continuum emission near the target surface. This fast ball then travels at constant velocity while it also expands at constant
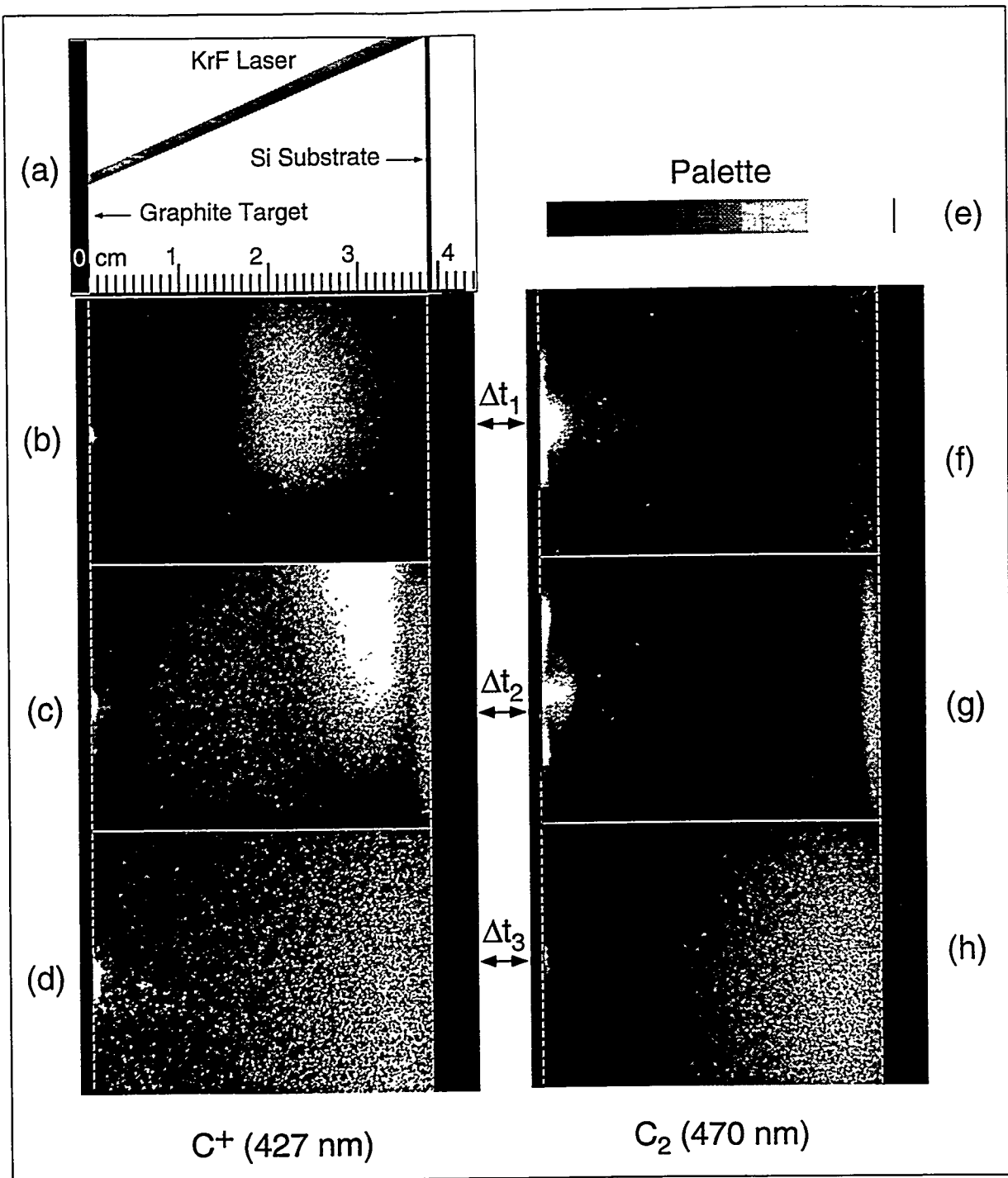
Fig.4. Species-resolved images of the KrF-laser (17 J/cm^2) generated plasma luminescence between a graphite target and an unheated silicon substrate, as shown schematically in (a). Images (b)-(d) are taken through a 427 nm filter (C$^+$ emission line) while images (f)-(h) on the right are taken through a 470 nm filter (C$_2$ ($\Delta v = +1$) Swan band). The pairs of images were acquired at the following times following the laser pulse: (b),(f) Δt_1 = 575-675 ns; (c),(g) Δt_2 = 775-975 ns; and (d),(h) Δt_3 = 10-12 μs. (e) Grayscale palette used for representation of the intensities.
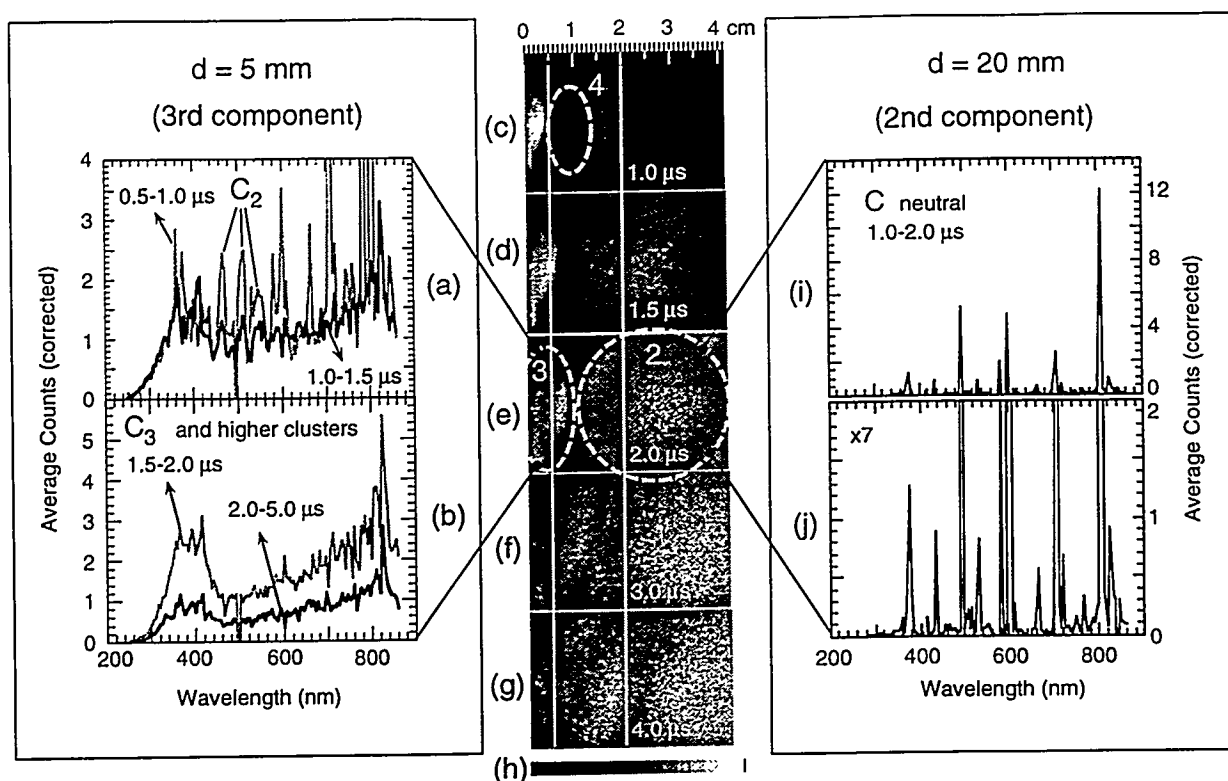
Fig. 5. Spectrally-corrected gated photon counting emission spectra of the carbon plume expansion into vacuum following KrF-laser (7 J/cm^2) ablation of pyrolytic graphite. As shown in the unfiltered ICCD images (c)-(g), two distances were chosen for study [(a),(b) d = 5 mm and (i),(j) d = 20 mm] in order to investigate the two regions of weak plasma luminescence demarcated in (e). Delays/exposures are (c) 1.0 μs/10 ns, (d) 1.5 μs/50 ns, (e) 2.0 μs/100 ns, (f) 3.0 μs/200 ns, (g) 5.0 μs/500 ns. As shown in (c), the jets of emission present at d = 5mm until Δt = 1.0 μs are comprised of C$_2$ emission bands (see gray curve in (a) 0.5–1.0 μs). The 3rd component emission spectrum is a broad continuum (see the three spectra in (a) and (b) for Δt > 1.0 μs) as it propagates across the d = 5 mm position (shown in (d)-(g)) with a distinguishable band of C$_3$ emission at 400 nm. Spectra (i) and (j) represent the emission collected from the 2nd component at d = 20 mm from 1.0–2.0 μs (as imaged in (c)-(e)). The spectra is entirely composed of atomic emission lines attributable to neutral C*. Spectrum (i) is replotted in (j) magnified by a factor of 7 to illustrate the absence of continuum emission at these times and distances. The gray scale palette used for imaging. Emission spectra were taken in the photon counting mode with a 5 nm increment, 25 shots/point, with monochromator slits of 1 mm and a dispersion of 0.5 nm/mm.

velocity. The center travels at v = 3.9 cm/μs (KE$_{C+}$ = 95eV) while the leading edge (defined as 10% of maximum intensity) travels at v = 5.5 cm/μs (KE$_{C+}$ = 190 eV) as shown in Fig. 3. Figure 3 traces the R-t behavior of the emission maxima (and first component leading edge) for both ArF and KrF-laser generated plasmas at 6.7 J/cm^2.

The asymmetry (tilt) of the fast ball, and the opposing tilt of the second component, appear correlated with the 30° incidence angle of the laser beam. As noted by Pappas et al., irradiation at large incident angles increases the deposition of laser energy into the plume due to the geometrical increase in optical path length at early times, which results in higher kinetic energies.[8] As this hotter material exits, it appears to exert a pressure back against the slower material near the target surface. This slower material is more apparent for KrF-laser generated plumes (see below, and Fig. 1(a),(b)) and results in a 'footprint' of laterally-expanding material along the target surface. This effect is very similar to the internal reflected shocks observed for graphite expansion into high

pressure background gases[18,19] except that the 'background gas' in this case is the carbon plasma itself. Similarly, the observed 'footprint' results in redeposited material around the irradiated spot.

The optical emission from this region is primarily from excited C_2 and, at later times, C_3, in agreement with the interpretation of clustering at the target surface due to counterpropagating atomic flows. These effects are illustrated in species-resolved images of the high-fluence, KrF-laser generated plasma luminescence [corresponding to full-spectrum image Fig. 1(a)] which are given in Fig. 4 for three time delays. The tunable filter was set to 427 nm (images on the left) in order to image the propagation of the fast ball of excited C^+ as it propagates across vacuum to collide with a silicon wafer at d = 3.9 cm. The images on the right investigate emission from excited C_2. Strong C_2 emission is observed in the laterally-expanding 'footprint' at the target surface. The weaker jets of emission [see Fig. 1(a) and 1(b)] extending 1–1.5 cm from the target in Fig. 4(f) and 4(g) are also due to C_2. And C_2 is again found in abundance at the substrate surface during the arrival and partial reflection of the fast component of the plume. This will be examined in detail below.

However, while in Fig. 4(b) the strong luminescence of the bright ball is easily attributed (from photomultiplier waveforms at 427 nm)[12] to excited C^+, the luminescence observed at the target and substrate surfaces in Figs. 4(c) and 4(d) is too weak to easily resolve. More importantly, this emission persists as the filter is tuned from the 427 nm C^+ line, indicative of a molecular band or continuum emission. Indeed at late times, weak luminescence is observed at all wavelengths as shown in Figs. 4(d) and 4(h). In order to dogmatically assign the luminescence from these different regions, combined imaging and gated photon counting spectroscopy were performed.

Figure 5 illustrates the combined imaging and photon counting measurements of the second and third plume components for KrF (7 J/cm²) laser-irradiated pyrolytic graphite in vacuum. A set of unfiltered ICCD images [Figs. 5(c)–5(g)] were used to spatially- and temporally-locate the second and third component of the plume during free expansion, as indicated in Fig. 5(e). For the second component, light at d = 2.0 (± 0.05) cm was collected from Δt = 1.0–2.0 μs after the laser pulse. As shown in Fig. 5 (i) and 5(j), the second ball of luminescence was found to contain many atomic lines from excited C* neutrals. No continuum emission was observed at this position and these times, as shown in the magnified spectrum of Fig. 5(j).

The third component was studied at d = 0.5 (±0.05) cm for the times indicated in Figs. 5(a) and 5(b). From 0.5–1.0 μs, the d = 0.5 cm position is immersed in the 'jets' noted as '4' in Fig. 5(c) and Fig. 1(b). The emission spectrum for this region consists of many bands of excited C_2 superimposed upon a continuum. By 1.0–1.5 μs, the 3rd component arrives at the d = 5 mm position, and the pronounced C_2 emission bands (radiative lifetime ~100 ns) cannot be observed in the broad continuum.

The noticeable blue band in the continuum (centered around 400 nm) is attributable to excited C_3 which is present for all times in this 3rd component, but is most pronounced during the passage of the bright front shown in Figs. 5(d) and 5(e). A similar progression from C_2 emission to C_3 / continuum emission was observed in the luminous 'footprint' traveling laterally along the target surface at higher KrF laser energy densities. Assignment of the broadband luminescence bands follows previous work in the literature.

The optical spectroscopy of small carbon clusters is reviewed by Weltner, Jr. and Van Zee.[20] Dimers can easily be identified in emission or absorption by using the Swan C_2 ($d^3\Pi_g$–$a^3\Pi_u$) system in the visible. The C_3 molecule has characteristic system of bands ($^1\Pi_u \rightarrow {}^1\Sigma_g$) with a 0–0 band at 405 nm which at high temperatures appears as a continuum due to large number of unresolved hot bands[20,21]. It should be mentioned that in emission this band can overlap with the Deslandres-d'Azambuja ($C^1\Pi_g \rightarrow A^1\Pi_u$) system[22] of C_2 that complicates an identification of C_3 clusters. Kratschmer et al. tentatively assigned absorption bands of higher carbon clusters in matrices in a progression across the visible spectrum[C_4 (247 nm), C_5 (311 nm), C_6 (394 nm), C_7 (447 nm0, C_8 (529 nm) and C_9 (586 nm)].[23] At high temperatures, a broadening of these bands should produce a continuum in the visible region. Larger clusters and nanoparticles eventually emit Planck blackbody continua, as studied by Rohlfing for carbon particles emitted by a laser vaporization cluster source.[24]

As shown in Fig. 4(g), another region of near-surface luminescence occurs when components (1) and (2) of the plume arrive at the substrate. Figures 6(a)–6(e) trace the formation of this emission with a sequence of ICCD photographs of luminescence at 470 nm (chosen to coincide with a (Δv = +1) C_2 Swan emission bandhead).
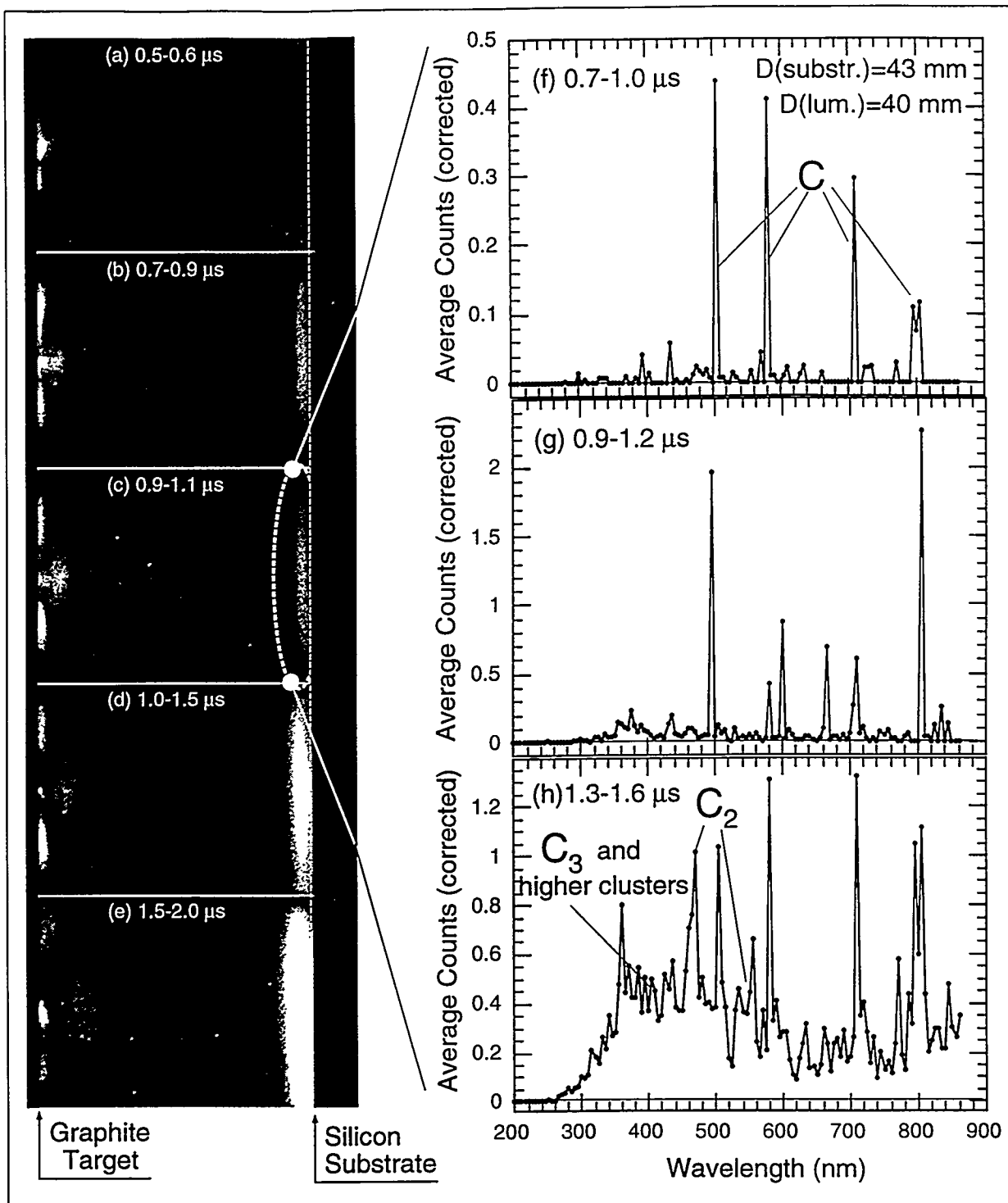
Fig. 6. (a)-(e) Species-resolved (λ = 470 nm ± 5 nm, C_2 Swan band emission) gated-ICCD images tracing the evolution of the near-substrate luminescence caused by the collision of the KrF-laser (17.7 J/cm^2) carbon plasma plume with an unheated Si (100) substrate in vacuum. The substrate is located at the thin dashed line. Also shown is the propagation of the 'footprint' luminescence along the target surface and the forward-expanding 3rd component at the left of the frame. The emission spectra at d = 4.0 cm (3 mm above the substrate surface) of the forming 'rebound' luminescence are given during (f) 0.7–1.0 μs, (g) 0.9–1.2 μs and (h) 1.3–1.6 μs, respectively. Arrival of the atomic 2nd component in (f) leads to the gas-phase formation of C_2 and C_3 above the substrate surface as evidenced by the emission spectrum (h), which is remarkably similar to that of the slow-moving 3rd component back near the target surface [see Fig. 5(a) and 5(b)].

Photon counting emission spectra of the weak 'rebound' luminescence were collected 3 mm above the silicon surface during film deposition and are shown in Figs. 6 (f)–6(h). The arrival of the fast ionic/atomic (1st and 2nd) components is indicated in Fig. 6(f) by the presence of only atomic carbon lines. As the luminescence 'rebounds' from the substrate surface and extends to the observation position, the atomic spectrum gives way [Fig. 6(g)] to bands of C_2, C_3, and continuum emission [Fig. 6(h)] very similar to that observed at comparable times in the 3rd component back at the target surface. However, this material is clearly formed by additional gas-phase collisions induced by the substrate, and not by the transport of the slow third component to these distances.

Clusters are thus observed at both the target and the substrate during plume expansion in vacuum. The near-substrate clusters appear correlated with plume collisions between carbon atoms in the fast atomic cloud, forming C_2, C_3 and higher clusters by monomer addition. The dynamics of the 'footprint' of near-target cluster-luminescence suggests that additional interplume collisions, caused by a backward-going flux of plume atoms, leads to the observed clustering and unique redeposition profile. The forward-going fraction of these clusters (3rd component in Fig. 3) continue to propagate toward the growing film (at $v_{peak} \sim 0.1$–0.3 cm/μs) to arrive, for example, at $d = 4$ cm at $t_{peak} \sim 13$–40 μs. It should be emphasized that both fluxes of clusters should be detected in mass-spectrometric measurements, and might be attributed to ejection from the graphite target.

Addition of an inert background gas results in greatly enhanced cluster production. This is evident from a large increase in continuum emission within the optical spectra, a bright region of luminescence on the ICCD images, and a third flux of positively-charged material arriving at the ion probe. Figure 7 illustrates the ion probe and imaging observations. A full description of the scattering and gas dynamic effects will not be detailed here. However the results are understandable from similar measurements of 'plume splitting' for other materials.[15–17]

As shown in Fig. 7, small additions of background gas attenuate the ion flux exponentially, but (for graphite in argon) do not slow the fast component. The fast component of the ion flux shown in Fig. 7(a) are carbon ions transmitted statistically without scattering. A second distribution of rapidly-slowing material 'splits' distinctly in time from the unscattered distribution [distribution peaking at 10–25 μs in Fig. 7(a)]. This material corresponds with plume atoms which have
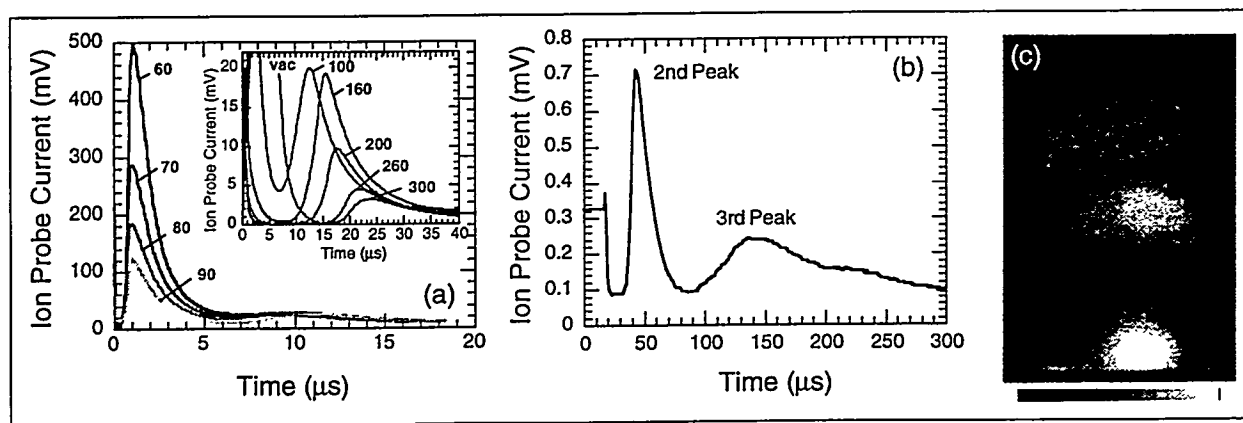

Fig.7. (a) Ion probe current (mV into 50 Ω) induced by the ArF-laser (7 J/cm^2) generated plasma at d = 5 cm along the normal to the graphite target into 60, 70, 80 and 90 mTorr of Ar. In addition to the dominant fast component of the ion flux, a second component is observable at delays of ~10 μs. The insert shows the disappearance of the fast component and the evolution of the second component for vacuum (7 × 10^{-7} Torr) and argon pressures of 100, 160, 200, 260, and 300 mTorr. (b) Ion current versus time after laser pulse in 350 mTorr of Ar. (c) ICCD image of luminescence (unfiltered) from the ArF-laser (6.0 J/cm^2) generated carbon plasma propagating into 70 mTorr of argon (2.1 μs delay, 0.2 μs exposure). The grayscale palette used is shown.

undergone scattering and momentum-transfer with the background gas and with each other, resulting in the formation of a well-defined shock front. At higher pressures, the first peak is completely attenuated and the first material to arrive is in the 'shock front' or second component.

In many cases, as in the carbon plume, clustering occurs due to the additional plume collisions induced by the counterpropagating plume atom-fluxes and by the confinement of the plume atoms within the 'bubble' of the snowplowed background gas.[18,19] This becomes observable as yet another well-separated peak in the ion probe signal at very late times [Fig. 7(b)], or by the arrival of broadband luminescence using the diagnostics described above. These diagnostic techniques have recently been applied to investigate doping of ZnTe films following KrF-laser ablation into N_2.[25–28]

For graphite ablation into 70 mTorr Argon [Fig. 7(c)], one should compare the plume to Fig. 1(c). Enhanced luminescence is observable on three fronts in Fig. 7(c): (1) the slowing (scattered) portion of the first component, (2) a front within the forward portion of the second component which appears to be interacting with this slowed first component, and (3) enhanced overall third-component emission.

While exact understanding of the complex scattering and gas dynamic effects await sophisticated modeling, the above diagnostic techniques and results provide clear evidence for the significance of interplume collisions (in *vacuum* as well as background gases) on the type of species and associated velocity distributions of material arriving to the growing film surface during pulsed laser deposition.

CONCLUSIONS

In this paper, key differences noted between KrF- and ArF-laser generated carbon plasmas under PLD film growth conditions of amorphous diamond were investigated using spectroscopic imaging and gated photon counting emission spectroscopy. Both lasers produced an expanding plasma containing the same three components: (1) a fast plasma ball of ion luminescence traveling (and also expanding) with constant velocity (ArF: v_{center} ~3.9 cm/μs (KE$_{C+}$ ~ 85 eV), $v_{expan.}$ ~1.6 cm/μs); (2) a second, broad ball of carbon neutral luminescence which travels at v ~ 1.0 cm/μs (KE$_C$ ~ 6 eV); and (3) a region of clusters (C_2, C_3, and higher) exhibiting emission bands and a continuum, traveling v ~ 0.1–0.3 cm/μs (KE$_{C_3}$ ~ 0.2–1.7 eV). However, ArF-generated plumes were higher in ionization and produced fewer clusters, yielding superior ta:C films. KrF-generated films also produced jets of luminescent C_2, more vapor, and significantly more cluster luminescence. In addition, the 'rebound' luminescence resulting from the collision of the plume with the substrate was investigated.

Easier production of the high energy C^+ luminescent ball, and the minimization of the slow cluster (3rd) component, appear to be the chief advantage offered by ArF (193 nm) laser irradiation over KrF (248 nm) for high quality ta-C films. This luminescent ball appears to result from coupling of the laser energy into the expanding vapor, heating the plasma by inverse Bremmstrahlung or more likely by photoionization.

Photoionization of atomic carbon from the ground state (I.P. 11.26 eV) is very unlikely since two-(ArF) and three-(KrF) photon nonresonant absorption is required. However, as reported by Pappas et al. for their work at 248 nm, a resonance exists between the carbon atom 3s ($^1P_1^o$) ← $2p^2$ ($^1S_0$) transition (247.93 nm) and the KrF laser line. For ArF-irradiation, another coincidence exists between the 3s ($^1P_1^o$) ← $2p^2$ ($^1D_2$) levels of carbon (at 193.09 nm). Given a population of these excited carbon levels, resonantly-enhanced two photon ionization should proceed in both cases since these transitions both fall within the respective spectral lineshapes of the laser transitions. However, while the ArF intensity at 193.09 nm is estimated at ~90% of the peak at 193.3 nm, the KrF intensity at 247.93 nm is estimated at only ~15% of the peak at 248.4 nm. This may help explain the greater ionization efficiency at 193 nm.

These levels [C($^1S_0$) (at 2.68 eV) and C($^1D_2$) (at 1.26 eV), in addition to the ground C(^3P) state] are the primary dissociation products of excited C_2. Dimers ejected from the target in the $a^3\Pi_u$ state may photodissociate into these excited atomic levels via the energetically possible C_2 d $^3\Pi_g$←a $^3\Pi_u$ transition from v=0 (ArF) or from higher vibrational levels (v''=6 for KrF). For C_2 excited by the laser plasma, more KrF photodissociation pathways become energetically allowed. Similar pathways could be argued for photodissociation of C_3.

The proposed C_2,C_3-photodissociation/C^*-photoionization mechanism for the production of the fast ion ball is possible given the recent work of Krajnovich who measured the primary ejecta from 248 nm-irradiated highly-oriented pyrolytic graphite (HOPG) targets at low (0.3–0.7 J/cm^2) energy densities.[29] Krajnovich found relative densities of $[C_3] > [C_1] > [C_2]$ at long distances normal to the target with a quadrupole TOFMS. The velocities converged to equal values (v_{mp} ~ 1.3 cm/μs) at the upper end of his fluence range, indicating gas dynamic interactions during the expansion, however principally the results indicated that the most abundant ejected species was C_3 which, along with C_2, acquired highly non-thermal energy somehow very near the surface.

Pappas et al.[8] also found highly non-thermal (12 eV, 1.0 cm/μs) C_2 using LIF in KrF (2.2 J/cm^2)-irradiated polycrystalline graphite plumes and suggested charge-exchange collisions in the expanding plasma may explain the nonthermal behavior. Monchicourt, in studies of 532-nm irradiation (200 MW/cm^2) of polycrystalline graphite, found that *excited* C_1^*, C_2^*, and C_3^* propagation velocities follow a 3:2:1 ratio and proposed that hot C atoms can form excited C_2^* and C_3^* clusters in binary associative collisions with slow C atoms or C_2 molecules.[30]

Our results lend insight into the role of interplume gas dynamics on the measured velocity distributions. Excited C_1^* and C_3^* (components 2 and 3 in Fig. 3 above) are observed to travel at ratios of 3.7: 1 and 11:1 for KrF and ArF, respectively. Excited C_2^* and C_3^* appear to form in stepwise order from collisions of fast atoms (components 1 and 2) with slow atoms and dimers in the gas phase near both target and substrate. Most important is the view afforded of the effects of gas dynamics on the measured distributions.

From the images, it seems clear that a hotter region of plasma is caused by laser absorption within the primary ejecta, resulting in a two-temperature plume from the start. The higher pressure in this hot-zone causes it to expand faster from the surface, and the surrounding vapor, leading to turbulent instabilities in the expansion of the remaining vapor. The 'footprint' of cluster luminescence along the target surface is a remnant of the backward pressure left from the expansion of the fast component.

The cluster luminescence serves as a signature of interplume collisions. The 'rebound' luminescence is attributable to dimers, trimers, and higher clusters which appear to form in stepwise order from counterpropagating fluxes of atomic vapor, one incoming and one reflected from the substrate surface. It is natural to assume that a similar process is responsible for a significant portion of the observed near-target 'footprint' of clusters. In this case, however, the 'incoming' flux to the surface is backward-going (redeposition) flux caused as a reaction to the ejection of the fast ion ball. The surprising general result is that two fluxes of clusters have been observed in *vacuum* due to interplume collisions.

The plume can be thought of as moving in a background gas of plume atoms. Plume expansion is typically modeled as a free expansion, where a distribution of velocities is set after a short distance and neighboring fluid elements have nearly zero relative velocities. In this case (and others) of a two-temperature plasma, different distributions within the plume exert relative pressures on one another. For example, the flat shape of the KrF ion ball in Fig. 1(a) may result from the greater amount of slower ejecta observed in this case, resulting in extra collisions on the trailing edge of the first component compared to ArF in Fig. 1(c).

Moreover, addition of a background gas understandably scatters the primary flux, with the slowed- remnants serving as additional 'background gas' for oncoming plume atoms. A shock front rapidly forms as material piles up due to nonlinear three-body collisional reaction rates. In the case of a multicomponent plume in vacuum (as we have here) several different fronts are evident from the outset . Confinement of the plume leads to clustering.

While scattering and shock-formation represent such obvious perturbations of the PLD flux arriving through a background gas, the sensitive diagnostics described here indicate the importance of interplume collisions on the type and velocity of species arriving to the substrate during film growth *in vacuum.*

ACKNOWLEDGMENTS

REFERENCES

1. D. R. McKenzie, D. Muller, and B. A. Pailthorpe, *Phys. Rev. Lett.* **67**, 773 (1991).

2. F. Davanloo, E. M. Juengerman, D. R. Jander, T. J. Lee, and C. B. Collins, *J. Appl. Phys.* **67**, 2081 (1990).

3. C. B. Collins, F. Davanloo, D. R. Jander, T. J. Lee, H. Park, and J. H. You, *J. Appl. Phys.* **69**, 7862 (1991).

4. F. Davanloo, T. J. Lee, D. R. Jander, H. Park, J. H. You and C. B. Collins, *J. Appl. Phys.* **71**, 1446(1992).;

5. C. B. Collins, F. Davanloo, T. J. Lee, H. Park, and J. H. You, *J. Vac. Sci. Technol. B* **11**, 1936 (1993).

6. J. J. Cuomo, D. L. Pappas, J. Bruley, J. P. Doyle, and K. L. Saenger, *J. Appl. Phys.* **70**, 1706 (1991).

7. D. L. Pappas, K. L. Saenger, J. Bruley, W. Krakow, J. J. Cuomo, T. Gu, and R. W. Collins *J. Appl. Phys.* **71**, 5675 (1992).

8. D. L. Pappas, K. L. Saenger, J. J. Cuomo, and R. W. Dreyfus, *J. Appl. Phys.* **72**, 3966 (1993).

9. F. Xiong, Y. Y. Wang, V. Leppert, and R. P. H. Chang, *J. Mater. Res.* **8**, 2265 (1993).

10. F. Xiong, Y. Y. Wang, and R. P. H. Chang, *Phys. Rev. B* **48**, 8016 (1993).

11. A. A. Puretzky, D. B. Geohegan, G. E. Jellison, Jr., and M. M. McGibbon, , in Film Synthesis and Growth Using Energetic Beams, edited by H. A. Atwater, J. T. Dickinson, D. H. Lowndes, A. Polman (Mat. Res. Soc. Symp. Proc. 388, Pittsburgh, PA, 1995), p. 145-150 .

12. A. A. Puretzky, D. B. Geohegan and , G. E. Jellison, Jr., and M. M. McGibbon, Proceedings of the Third International Conference on Laser Ablation COLA'95/EMRS (Strasbourg France, May 1995), *Appl. Surf. Science* (in press).

13. D. B. Geohegan, *Appl. Phys. Lett.* **60**, 2732 (1992).

14. David B. Geohegan, in Laser Ablation in Materials Processing: Fundamentals and Applications, edited by B. Braren, J. Dubowski, and D. Norton, (Mat. Res. Soc. Symp. Proc. 285 , Pittsburgh, PA, 1993), p. 27-32.

15. D. B. Geohegan and A. A. Puretzky, *Appl. Phys. Lett.* **67**, 197 (1995).

16. D. B. Geohegan and A. A. Puretzky, in Film Synthesis and Growth Using Energetic Beams, edited by H. A. Atwater, J. T. Dickinson, D. H. Lowndes, A. Polman (Mat. Res. Soc. Symp. Proc. 388, Pittsburgh, PA, 1995), p. 21–26.

17. D. B. Geohegan and A. A. Puretzky, Proceedings of the Third International Conference on Laser Ablation COLA'95/EMRS (Strasbourg France, May 1995), *Appl. Surf. Science* (in press).

18. D. B. Geohegan, A. A. Puretzky, R. L. Hettich, X.-Y. Zheng, R. E. Haufler, and R. N. Compton, p.349 in *Advanced Materials '93, IV/ Laser and Ion Beam Modification of*

Materials, edited by I. Yamada et al., IUMRS-ICAM Conference , Trans. Mat. Res. Soc. Jpn., Volume 17, (1994).

19. A. A. Puretzky, D. B. Geohegan, R. E. Haufler, R. L. Hettich, , X.-Y. Zheng, and R. N. Compton, in Laser Ablation: Mechanisms and Applications II, edited by J.C. Miller and D.B. Geohegan, *Amer. Inst. of Physics Conf. Proc.* 288 : (Amer. Inst. of Physics, New York , 1994), p. 365.

20. W. Weltner, Jr. and R. J. VanZee, *Chem. Rev.* **89**, 1713 (1989).

21. *Spectra of Diatomic Molecules* by G. Herzberg, Van Nostrand, New York, 1950.

22. *The Identification of Molecular Spectra*, 4th ed., by R. W. B. Pearse and A. G. Gaydon, (Chapman and Hall, London, 1984), p.85.

23. W. Kratschmer, N. Sorg, and D. R. Huffman, *Surface Science* **156**, 814 (1985).

24. E. A. Rohlfing, *J. Chem. Phys.* **89**, 6103 (1988).

25. D. H. Lowndes, C. M. Rouleau, D. B. Geohegan, A. A. Puretzky, M. A. Strauss, A. J. Pedraza, J. W. Park, J. D. Budai, and D. B. Poker, "Pulsed Laser Ablation Growth and Doping of Epitaxial Compound Semiconductor Films," in *Advanced Laser Processing of Materials–Fundamentals and Applications,"* Materials Research Society Meeting, 1995 (this proceeding).

26. C. M. Rouleau, D. H. Lowndes, M. A. Strauss, S. Cao, A. J. Pedraza, D. B. Geohegan, A. A. Puretzky, and L. F. Allard, "Effect of Ambient Gas Pressure on Pulsed Laser Ablation Plume Dynamics and ZnTe Film Growth," in *Advanced Laser Processing of Materials–Fundamentals and Applications,"* Materials Research Society Meeting, 1995 (this proceeding).

27. Douglas H. Lowndes, C. M. Rouleau, J. W. McCamy, J. D. Budai, D. B. Poker, D. B. Geohegan, A. A. Puretzky, and Zhen Zhu, p. in Film Synthesis and Growth Using Energetic Beams, edited by H. A. Atwater, J. T. Dickinson, D. H. Lowndes, A. Polman (Mat. Res. Soc. Symp. Proc. 388, Pittsburgh, PA, 1995), p. 85–90.

28. C. M. Rouleau, D. H. Lowndes, J. W. McCamy, J. D. Budai, D. B. Poker, D. B. Geohegan, A. A. Puretzky, and S. Zhu, *Appl. Phys. Lett.* **67**, 2545 (1995).

29. D. J. Krajonovich, *J. Chem. Phys.* **102**, 726 (1995).

30. P. Monchicourt, *Phys. Rev. Lett.* **66**, 1430 (1991).

DISCLAIMER